

Quantum transport signature of strain-induced scalar and pseudovector potentials in a crenelated *h*-BN/graphene heterostructure

Romaine Kerjouan¹, Michael Rosticher,¹ Aurélie Pierret,¹ Kenji Watanabe², Takashi Taniguchi²,³ Sukhdeep Dhillon,¹ Robson Ferreira,¹ Daniel Dolfi,⁴ Mark Goerbig,⁵ Bernard Plaçais¹, and Juliette Mangeney^{1,*}

¹ Laboratoire de Physique de l'Ecole Normale Supérieure (ENS), Université Paris Sciences et Lettres (PSL), CNRS, Sorbonne Université, Université de Paris, Paris, France

² Research Center for Functional Materials, National Institute for Materials Science, 1-1 Namiki, Tsukuba 305-0044, Japan

³ International Center for Materials Nanoarchitectonics, National Institute for Materials Science, 1-1 Namiki, Tsukuba 305-0044, Japan

⁴ Thales Research & Technology, Thales Group, 91120 Palaiseau, France

⁵ Laboratoire de Physique des Solides, CNRS, Université Paris-Saclay, 91400 Orsay, France

(Received 16 February 2024; revised 11 June 2024; accepted 5 August 2024; published 30 August 2024)

The sharp Dirac cone of electronic dispersion confers to graphene a remarkable sensitivity to strain. It is usually encoded in scalar and pseudovector potentials, induced by the modification of hopping parameters, which have given rise to new phenomena at the nanoscale, such as giant pseudomagnetic fields and valley polarization. Here, we unveil the effect of these potentials on the quantum transport across a succession of strain-induced barriers. We use high-mobility *h*-BN-encapsulated graphene, transferred over a large ($10 \times 10 \mu\text{m}^2$) crenelated *h*-BN substrate. We show the emergence of a broad resistance ancillary peak at positive energy that arises from Klein-tunneling barriers induced by the tensile strain at the trench edges. Our theoretical study, in agreement with experiment, quantitatively highlights the balanced contributions of strain-induced scalar and pseudovector potentials on ballistic transport. Our results establish crenelated van der Waals heterostructures as a promising platform for strain engineering in view of applications and basic physics.

DOI: 10.1103/PhysRevApplied.22.024076

I. INTRODUCTION

Graphene exhibits high mechanical flexibility and remarkable electronic properties, making it an ideal platform for strain engineering to explore novel fundamental phenomena and to realize straintronic devices [1,2]. Elastic strain gives rise to two primary effects in the low-energy band structure of graphene: shifts in the energy of the Dirac point, which is typically incorporated as a scalar potential, and shifts in the momenta of the Dirac cones in opposite directions for the two valleys, often described by a pseudovector potential [3–11]. Strained graphene has been the subject of a large number of studies, revealing fascinating physical phenomena that depend mainly on whether the strain is nonuniform or not. Nonuniform strains over typically a few nanometers create in graphene giant pseudomagnetic fields that can reach several hundreds of tesla [12], giving rise to the pseudomagnetic quantum Hall effect [13] and the proposals of valley-splitting topological

channels for chiral fermions [14] or the appearance of a superconductive state [15,16]. Such nonuniform strain has been obtained on localized curved structures such as wrinkles or bubbles [13,17–19] and, recently, on a large scale using twisted multilayers [13] and substrate nanopatterning [14,20–22], making it possible to study the pseudomagnetic field using magnetotransport measurements [13,23]. Uniform strain, on the other hand, creates large scalar potentials that modify the graphene work function [24]. By achieving uniform strain in mesoscopic graphene devices, strain-induced scalar potentials have been probed using transport experiments [25,26]. In spite of intensive work, the investigation of the quantum transport of Dirac fermions through a network of uniform strained barriers remains elusive in graphene.

Probing the quantum transport of relativistic electrons in graphene through a strained barrier is of considerable interest, as it differs remarkably from transport across an electrostatic barrier, such as a *p-n-p* junction [27]. For instance, Dirac fermions undergo Klein tunneling across an electrostatic barrier and those at normal incidence,

*Contact author: juliette.mangeney@phys.ens.fr

constrained to retain their transverse momentum, $k_{\perp} = 0$, and forbidden to scatter directly backward, penetrate the barrier with unit probability. In contrast, the pseudovector potential in strained graphene, which is absent in electrostatically defined n - p - n junctions, shifts the transverse momentum, $k_{\perp} \rightarrow k_{\perp} - A_{\perp}$, of electrons inside the barriers, affecting the quantum transport of electrons, which is sensitive to both energy and momentum conservation. For instance, partial reflections for carriers normally incident on the strained junction are predicted. This effect, which is specific to ballistic graphene, is irrelevant in diffusive graphene, where momentum recoil is supplied by impurities.

Furthermore, it is worth pointing out that quantum transport of electrons in graphene through a network of uniform strained barriers is a somewhat unusual situation in which the pseudovector potential has a physical significance. This would not be the case in systems with a homogeneous strain, in which the global shift $k_{\perp} \rightarrow k_{\perp} - A_{\perp}$ of the positions of the Dirac points inside the first Brillouin zone has no physical consequence and could be compensated by a global gauge choice of the vector potential. Such a global gauge choice is prohibited for a succession of strained- and unstrained-graphene regions. On the other hand, pseudomagnetic fields associated with the curl of the vector potential are expected to play no essential role in the quantum transport of electrons through a network of uniform uniaxial strained barriers. Indeed, such pseudomagnetic fields and the associated Landau quantization require a broken inversion symmetry between the two graphene sublattices, as is the case in the particular strain patterns with a $2\pi/3$ -rotation symmetry observed in scanning-tunneling-spectroscopic experiments [12]. Apart, perhaps, from few localized impurities, the pseudomagnetic field therefore has a negligible contribution to quantum transport across a uniaxial strained-graphene barrier, while the pseudovector-potential contribution, which vanishes in diffusive graphene, is expected to dominate the ballistic transport. Quantum transport across a uniform strained barrier can thus serve as a highly sensitive probe of strain-induced pseudovector potentials, which have been little studied compared to pseudomagnetic fields.

Here, we report on a mechanically robust strained-graphene mesoscopic device made of a crenelated van der Waals h -BN/graphene heterostructure. Our approach relies on transferring a high-quality graphene layer, protected by a thin h -BN layer, on a crenelated h -BN substrate to create a periodic network of strained and unstrained regions. The strained regions act as barriers for ballistic electrons and thus, in the device, electrons propagate through a succession of strain barriers. We probe the Klein-tunneling properties of ballistic electrons across the strain-induced barriers using low-temperature transport measurements and model them by combining elasticity and tight-binding theories with Dirac fermion optics and Landauer-Buttiker

scattering approaches. We unveil a signature of tensile strain in the form of a large and broad ancillary resistance peak at a positive energy. We show that the peak amplitude and shape result from balanced contributions of scalar and pseudovector potentials in the Klein-tunneling strained barriers.

II. MESOSCOPIC TRANSPORT ACROSS A CRENELATED h -BN/GRAPEHENE HETEROSTRUCTURE

The device [Fig. 1(a)] is made of a ($L \times W = 12 \times 8 \mu\text{m}$) exfoliated monolayer graphene protected by a thin h -BN layer and transferred onto a 62-nm-thick h -BN layer nanopatterned in periodic trenches of depth 35 nm, resting on a silicon substrate with 500 nm of oxide (SiO_2) used as a back-gate dielectric [see Fig. 1(b) and Appendix A for the fabrication process]. Due to strong van der Waals interactions, the h -BN/graphene heterostructure adheres to the crenelated h -BN substrate at the top and bottom of the slot, as shown in the atomic force microscopy (AFM) image [Fig. 1(c)]. This anchors minimally strained regions concentrating the tensile strain in the suspended graphene region connecting the two anchored regions; its length is determined by the balance between the out-of-plane component of the tension and the h -BN adhesion force. Thus, our approach yields 300-nm-long regions of unstrained graphene on top and 400-nm-long regions in the bottom, and typically 150-nm-long regions of tensile-strained graphene along the trenches. If we assume uniform uniaxial strain in the tilted regions that are uniformly strained with a uniaxial stress, we can estimate the strain value in these tilted regions by $\varepsilon_{\text{global}} = \sqrt{(1 + (dH/L_{\text{tilted}})^2)} - 1 = 2.7\%$, with $dH = 35 \text{ nm}$ and $L_{\text{tilted}} = 150 \text{ nm}$, extracted from the AFM measurements [see Fig. 1(c)]. Thus, AFM measurements combined with basic geometrical considerations indicate the strain in our device to be a few percent. We infer high electronic mobility in the graphene on the top of the crenelation, as the h -BN/graphene heterostructure is anchored to pristine h -BN [28], and in the tensile-strained region because the graphene is suspended [29]. In contrast, in the bottom of the crenelation, the quality of the graphene is degraded by the etched h -BN substrate, which suppresses high carrier mobility. Quantum transport across an N -crenelated device can thus be regarded as the sum of the N diffusive sections and $2N$ strained junctions in series. Note that due to cleaning by sonication, the softness of the etched h -BN remains sufficient to ensure strong van der Waals adhesion of the h -BN/graphene heterostructure. The Raman spectroscopy in Fig. 1(d) confirms the relatively high quality of the graphene, as the average intensity of the $2D$ peak, I_{2D} , is 2.5 times higher than that of the G peak, I_G , and the average intensity of the D peak, I_D , remains 3 times lower than that of the G peak [30]. Note that the I_{2D}/I_G

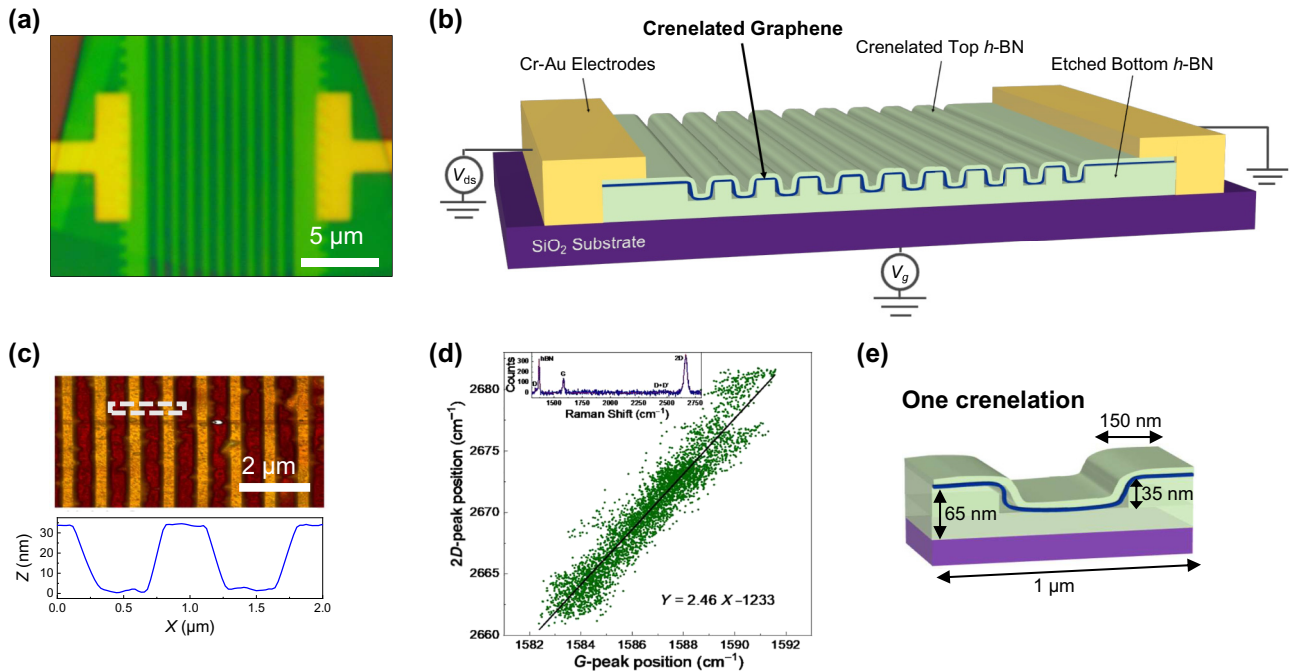


FIG. 1. The crenelated *h*-BN/graphene heterostructure: an optical image (a) and schematic drawing (b) of the crenelated *h*-BN/encapsulated graphene transistor. (c) Upper: an atomic force microscopy (AFM) image showing that the *h*-BN/graphene heterostructure sticks to the crenelated *h*-BN substrate at the top and bottom of the slot. Lower: a line-cut profile showing that the amplitude of the trench depths is typically 35 nm. (d) In green, the positions of the 2D peaks as a function of the positions of the *G* peaks over all the corrugated area, demonstrating clear correlation. The linear regression, in black, indicates a slope of 2.46, which is typical of the presence of strain in graphene. The inset shows a typical Raman spectrum of our device: blue line, experimental data; dashed red line, fit with five Lorentzians that are characteristic of graphene—peaks *D*, *G*, *D* + *D'*, and 2*D*—and of *h*-BN—peak *h*-BN. (e) A schematic drawing of one crenelation that includes a two 150-nm-long regions of high-quality unstrained graphene on top and one 400-nm-long region in the bottom, and two approximately 150-nm-long regions of tensile-strained graphene along the trenches.

ratio, which can be considered as a measure of graphene quality, follows the same periodicity as the crenelation, with high-ratio bands at the top regions and low-ratio bands at the bottom regions. This behavior supports our assumption of a high-quality graphene on the top of the crenelation, where the *h*-BN has only been exfoliated, and a low-quality graphene on the bottom of the crenelation, where the *h*-BN has been etched prior to graphene transfer. In addition, the positions of the 2*D* and *G* peaks over the crenelated device are clearly linearly correlated [see Fig. 1(d)] and the slope of the linear regression is 2.46, which is typical of the presence of strain in graphene [31,32], confirming the presence of strained regions in crenelated *h*-BN-encapsulated graphene. The existence of strained regions is further validated by deconvolving the Gaussian beam from the Raman spectra, which reveals a splitting of the 2*D* Raman peak, a signature of uniaxial strain in graphene, as detailed in the Supplemental Material [33]. The whole device includes $N = 10$ periodic crenelations [period $l = 1 \mu\text{m}$ length; see Fig. 1(e)] contributing additively to the total resistance. They are separated from the source and drain “edge contacts” by two unstrained-graphene regions of $1 \mu\text{m}$ length, which add a diffusive

contribution to the total resistance [34]. The large thickness of the SiO_2 with regard to the *h*-BN trench depth results in a modest modulation of the gate capacitance within the whole structure, between $C_{\text{bottom}} = 6.3 \times 10^{-9} \text{ F cm}^{-2}$ and $C_{\text{top}} = 5.9 \times 10^{-9} \text{ F cm}^{-2}$, i.e., <7% (here, we use $\epsilon_{\text{h-BN}} = 4.2$ [35]). Therefore, the modulation of the carrier density by the global back gate is relatively uniform over the entire device.

The signature of strain on transport is displayed in Fig. 2(a), which reports the low-bias differential resistance R_{ds} of the device as a function of the gate voltage V_g for different temperatures ranging from 4.2 K to 100 K. The $R_{\text{ds}} - V_g$ transport characteristics reveal a broad and large ancillary resistance peak at positive energy (chemical potential $\mu_{\text{peak}} = +163 \text{ meV}$ for $V_g = 62 \text{ V}$) in addition to the usual sharp charge-neutrality peak (at $V_g = 2 \text{ V}$). The Dirac peak [illustrated by the dashed blue curve in Fig. 2(a)] corresponds to the charge-neutrality point of the unstrained-graphene region and its position close to 0 V confirms the high quality of the graphene layer. The broad ancillary peak [illustrated by the dashed red curve in Fig. 2(a)], which does not exist in flat graphene, has an amplitude larger than that of the Dirac peak and a high

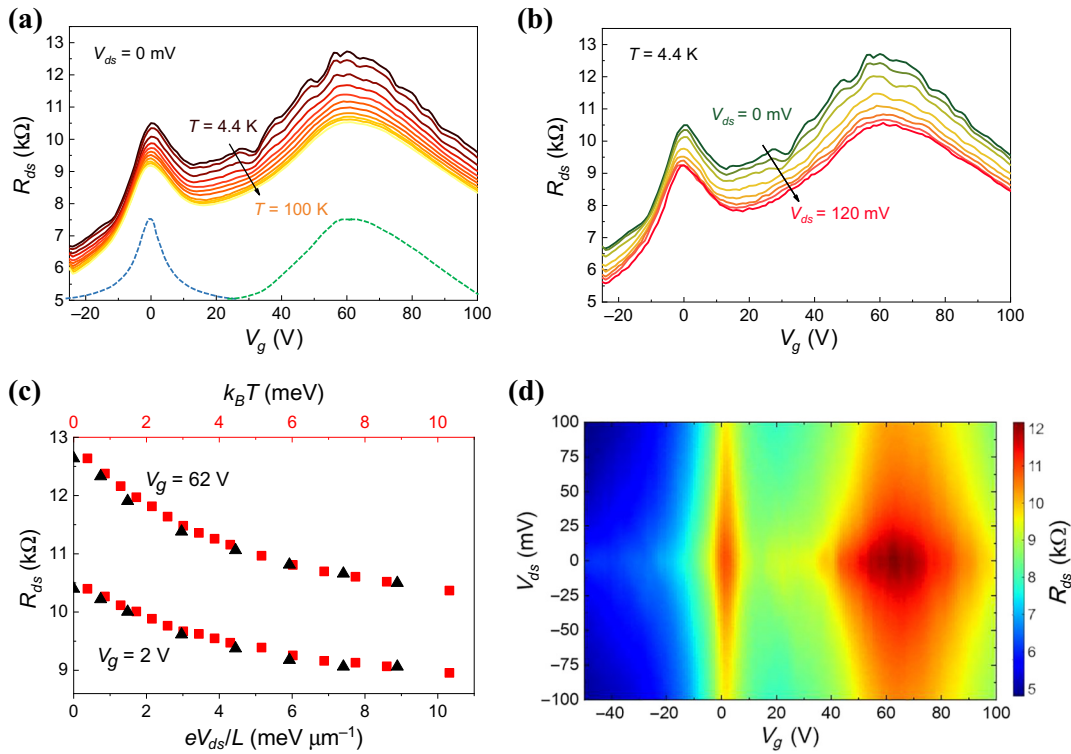


FIG. 2. The low-bias transport measurements. (a) The low-bias resistance R_{ds} measured at $V_{ds} = 10$ mV for different temperatures ($T = 4.4, 10, 20, 30, 40, 50, 60, 70, 80, 90$, and 100 K). We observe the emergence of a broad ancillary resistance peak at high V_g (illustrated by the dashed green curve) in addition to the usual Dirac peak (illustrated by the dashed blue curve). (b) The evolution of the R_{ds} - V_g characteristics at $T = 4.4$ K for different bias ($V_{ds} = 0, 10, 20, 40, 60, 80, 100$, and 120 mV). (c) R_{ds} as a function of the bias drop per micrometer (black symbols) and of the thermal energy (red symbols) close to the Dirac point ($V_g = 2$ V) and at the ancillary peak ($V_g = 62$ V). (d) A map of the differential resistance R_{ds} as a function of the gate voltage V_g and of the bias voltage V_{ds} at $T = 4.4$ K.

energy position, suggesting the presence of large potential barriers (μ_{peak}) induced by the tensile strains in the device. We note that the ancillary peak shape is in itself a signature of strain, as it differs significantly from standard Dirac peaks [36] or Dirac fermion reflector plateaus [37,38]. Moreover, we observe modulations, more visible in the gate-voltage range around the ancillary peak, that are unexpected in flat-graphene transistors. These modulations can be considered as hints of ballistic transport, as they are reminiscent of the electronic Fabry-Perot oscillations observed in electrostatic barriers [39]. Their characteristic energy separation is $\Delta E \approx 10$ meV, corresponding to an effective cavity length $L_{\text{cavity}} = 2\pi\hbar v_F / \Delta E = 360$ nm [40]. This length is consistent with the geometric length of the unstrained high-quality graphene at the top of the crenelation (approximately 300 nm). We therefore attribute the observed oscillations to Fabry-Perot interference between two strain-induced barriers (the regions of tilted graphene), with the top flat-graphene regions being considered as cavities for high-mobility carriers and strain junctions as efficient barriers. We can exclude Fabry-Perot oscillations within the barrier due to the length mismatch and the robustness of the oscillations at the ancillary peak.

The quantum nature of the resistance oscillations is corroborated by the temperature effect, which shows strong oscillation damping as the temperature increases. The blurring of interference resulting from quantum transport by the thermal broadening of the electrons impinging on the barriers is expected to follow an exponential suppression given by $\exp(-4\pi^2 k_B T / \Delta E)$, where k_B the Boltzmann constant and T is the temperature [41]. Considering our characteristic energy separation, a 95% drop in interference visibility corresponds to a thermal energy of $k_B T = 3$ meV, i.e., $T = 35$ K, which is in excellent agreement with our data. This observation confirms that the observed conductance oscillations arise from quantum interference of electrons propagating ballistically between strain barriers.

To gain deeper insight into the transport of ballistic electrons through strained-graphene barriers, we measure the evolution of the R_{ds} - V_g characteristics for different bias voltages V_{ds} —from 0 mV to 120 mV—at low temperature (4.4 K). With increasing bias, we observe in Fig. 2(b) that R_{ds} decreases and the Fabry-Perot oscillations vanish and cancel above 30 mV. Comparatively, the behavior of R_{ds} with temperature and bias is thus very similar. More

quantitatively, in Fig. 2(c) we report R_{ds} as a function of the bias drop per micrometer (black symbols) and of the thermal energy (red symbols) close to the Dirac point ($V_g = 2$ V) and at the ancillary peak ($V_g = 62$ V). The very good overlap between the two trends indicates that the device can be considered as 1- μm -long elements associated in series and thus supports our interpretation of the voltage drop in terms of N crenulations that contribute additively to the mesoscopic transport in our device. The differential resistance map as a function of V_g and V_{ds} is presented in Fig. 2(d). This two-dimensional (2D) plot highlights the strength and robustness of the ancillary peak, attributed to the propagation of ballistic electrons through the multiple strained-graphene barriers.

III. THEORETICAL DESCRIPTION OF ELECTRONIC TRANSPORT ACROSS A STRAINED-GRAPHENE BARRIER

In the following, we develop a theoretical description of quantum transport in this crenelated geometry combining elasticity and tight-binding theories, with Dirac fermion optics and Landauer-Buttiker scattering approaches. More specifically, we calculate the transmission and conductance through a single strained-graphene barrier surrounded by unstrained-graphene regions (see the Supplemental Material [33]). Let us start by calculating the electronic properties of strained graphene. We assume that the stress is uniaxial and collinear with the direction of electronic transport. We introduce the uniaxial strain tensor in the graphene lattice coordinates, $\bar{\varepsilon}(\varepsilon, \theta)$, where ε is the longitudinal deformation and θ is the angle between the strain direction and the zigzag crystallographic direction of the graphene sheet. A first effect of uniaxial strain on the graphene band structure is a shift in energy, independent of the valley, which arises from changes in the next-nearest-neighbor hopping parameter [42–44]. This effect can be described by an effective scalar potential, $\Delta V_{\text{strain}} = g_{\text{strain}}\varepsilon(1 - \sigma)$, where $g_{\text{strain}} \approx 3$ eV [45–47] and $\sigma = 0.165$ is the Poisson ratio [8,48]. In addition, the uniaxial strain modifies the interatom distances between nearest neighbors, δ'_i , and, as a consequence, the hopping amplitudes among neighboring sites change as

$t = t_0 \exp(-\beta(|\delta'_i(\varepsilon, \theta)|/a - 1))$, where $\beta = 3.37$ [9], $t_0 = 2.7$ eV, and $a = 0.24$ nm the lattice constant. In Fig. 3(a), we show the calculated low-energy dispersion and Fermi circle around the Dirac point for valleys K and K' in strained graphene with $\varepsilon = 2\%$ and a typical $\theta = 0^\circ$. Each Dirac cone of strained graphene, K_i , shifts away from its unstrained high-symmetry position by a wave vector $\Delta\mathbf{q}_{K_i}(\varepsilon, \theta)$. Note that the three couples of cones go through a different displacement but only one of them belongs to the first Brillouin zone and then takes part in the electronic transport to be considered here. Formally, the strain-induced momentum displacements of the Dirac

cones have the same effect as the application of a pseudovector potential, $\mathbf{A}_{K/K'}$, which shifts the Dirac cones away from the K and K' points in opposite directions in the reciprocal space ($\eta = +$ for the K valley and $\eta = -$ for the K' valley). The low-energy Hamiltonian at each Dirac cone can thus be written as

$$H = v_F \sigma (\mathbf{p} + e\mathbf{A}_{K/K'}) + \Delta V_{\text{strain}}, \quad \text{with} \\ \mathbf{A}_{K/K'} = \frac{-\eta \hbar \Delta \mathbf{q}_{K/K'}(\varepsilon, \theta)}{e}, \quad (1)$$

in which v_F is the Fermi velocity in graphene, σ is the pseudospin operator, and $\mathbf{p} = \hbar\mathbf{k}$ is the momentum operator. Note that we disregard changes in the magnitude and isotropy of the Fermi velocity, which is a fair approximation at moderate strain [8]. We conclude that the effect of strain on graphene leads to both a scalar potential ΔV_{strain} and a vector potential $\mathbf{A}_{K/K'}$, which turn out to be equally important in the analysis of our transport measurements.

We now compute the transmission probability of an electron through a strained-graphene barrier, as illustrated in Fig. 3(b), by continuity of the electronic wave functions at the strained-unstrained interfaces [9,49]. In Fig. 3(c), we show the calculated transmission probability $T(E, \phi)$ through a 150-nm-long strained barrier for $\varepsilon = 2\%$ and $\theta = 0^\circ$ as function of the electron energy E and its incidence angle ϕ upon the barrier. Note that the momentum displacement parallel to the direction of transport in strained graphene, Δq^{\parallel} , generates only an unimportant global phase on the wave functions. By contrast, the transverse component Δq^{\perp} , encoding the vector potential A^{\perp} and involved in the momentum conservation at the strained-unstrained interfaces, directly affects the Fresnel coefficients of the electronic transport. To cross the barrier, the incident angle of the electron has to obey the modified Snell-Descartes law (see the Supplemental Material [33]):

$$\frac{ev_F A_{K/K'}^{\perp}}{|E|} + \frac{|E - \Delta V_{\text{strain}}|}{|E|} \geq \sin \phi \geq \frac{ev_F A_{K/K'}^{\perp}}{|E|} - \frac{|E - \Delta V_{\text{strain}}|}{|E|}. \quad (2)$$

Equation (2) highlights the respective roles of ΔV_{strain} and $A_{K/K'}^{\perp}$ in the angular limits of the total internal reflection. In particular, the angular transmission window is pinched for $E = V_{\text{strain}}$ at a finite angle entirely prescribed by $ev_F A_{K/K'}^{\perp}/\Delta V_{\text{strain}}$. This strain-induced lifting of the valley degeneracy exists in principle but gives rise to nonlocal effects that are lost in our two-terminal experiment. In general, one can distinguish from Eq. (2) two limiting cases: (i) the vector-potential-dominated case ($|ev_F A_{K/K'}^{\perp}/\Delta V_{\text{strain}}| \gg 1$), in which tunneling across the barrier is cancelled and graphene becomes insulating in a

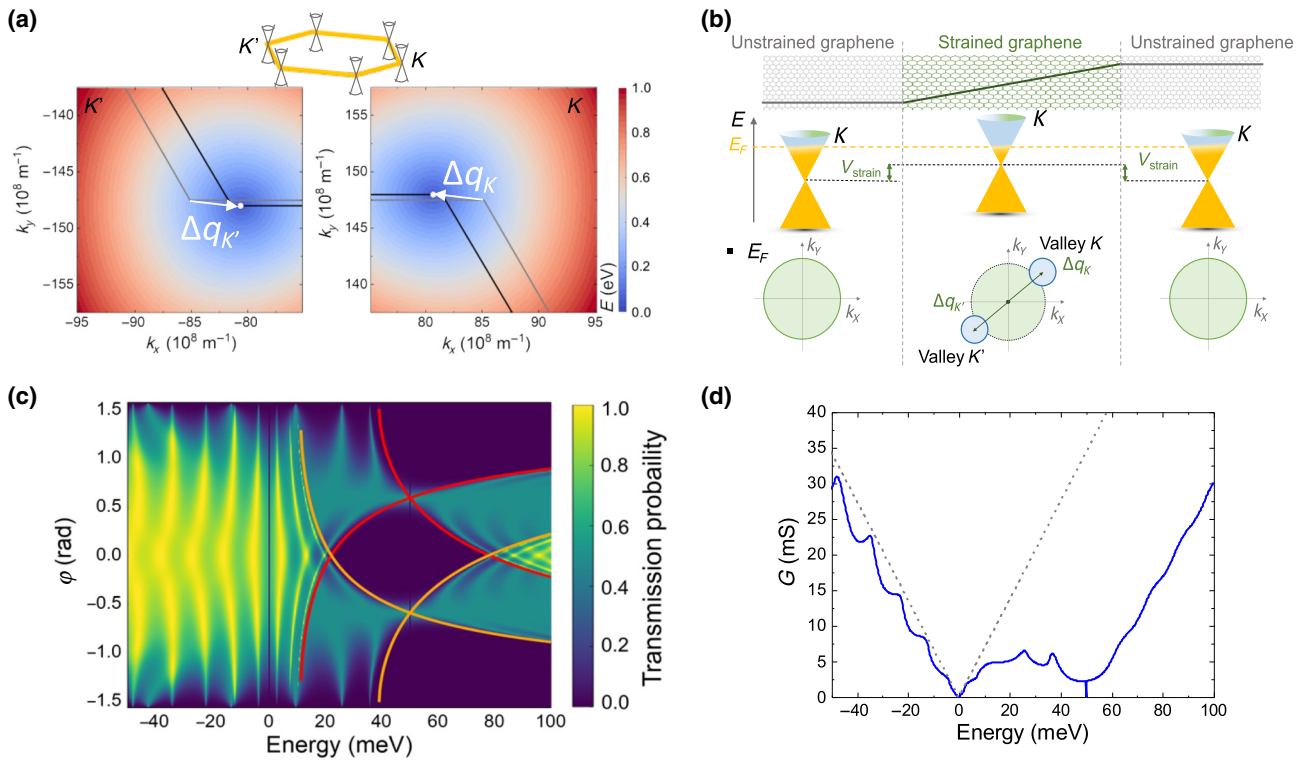


FIG. 3. Transport across a barrier of strain graphene. (a) The low-energy electronic dispersions for valleys K and K' for a uniaxial strain $\varepsilon = 2\%$ applied in direction $\theta = 0^\circ$ (the angle between the strain direction and the zigzag crystallographic direction of the graphene sheet). When compared to unstrained graphene, the Dirac cones are shifted by $\Delta q_{K/K'}$ in opposite directions for valleys K and K' . (b) A schematic of a barrier of strained graphene—the presence of an effective scalar potential ΔV_{strain} and of an effective vectorial pseudopotential $\mathbf{A}_{K/K'}$ of opposite direction according to the electron valley. (c) The transmission probability ($T = |t|^2$) through a 150-nm-long strain barrier with uniaxial strain $\varepsilon = 2\%$ in the direction $\theta = 0^\circ$ as a function of E , the electron energy, and φ , its incidence angle on the barrier. The effective pseudopotential induces changes in momentum conservation. The red lines correspond to the limits of the authorized incident angles for valley K and the orange ones for valley K' . (d) The ballistic conductance G for the same barrier with 8-μm width as a function of the electron energy. There are two minima: the first, at $E = 0$, is due to the zero electronic density of undoped graphene and the second, at $E = \Delta V_{\text{strain}}$, is due to the decrease of the authorized angles at this energy.

broad range of energy, making it an effective on-off transistor [50]; and (ii) the scalar-potential-dominated case ($|ev\mathbf{A}_{K/K'}^\perp/\Delta V_{\text{strain}}| \ll 1$), which is reminiscent of a conventional p - n junction [1,51]. An asset of our device is that it lies in the intermediate regime where both effects contribute constructively. It is important to point out that, in this intermediate regime, the quantum transport across strained barriers differs significantly from that through an electrostatic barrier, with notably a nonzero reflection for carriers normally incident ($\phi = 0$) on strained barriers due to the pseudovector potential in the strained region [see Fig. 3(c)]. Also, the resonance condition in the barrier depends not only on the barrier length and the scalar potential V_{strain} , similarly to the case of an electrostatic barrier, but also on the vector potential $\mathbf{A}_{K/K'}$, which is given by ϵ and θ , and on the valley, making it very different from that of an electrostatic barrier.

Finally, we calculate the conductance G of electrons in graphene propagating across a strained-graphene barrier at zero bias and low temperature from the

electron-transmission probability, using the Landauer-Buttiker formalism (see the Supplemental Material [33]). In Fig. 3(d), we report the conductance of a single strained-graphene barrier of width 8 μm and length 150 nm with $\varepsilon = 2\%$ and a $\theta = 0^\circ$. The conductance G presents the expected minimum at the charge-neutrality point ($E = 0$) as well as a second minimum at $E = \Delta V_{\text{strain}}$ due to few incident angles being allowed to cross the strain barrier at around this energy.

IV. ORIGIN OF THE ANCILLARY RESISTANCE PEAK

Finally, for direct comparison with the experimental data, we compute the resistance of the whole strained-graphene device by calculating the resistance of a single crenelation, which consists of two strained barriers, and multiplying this resistance by a factor $N = 10$ for additive contribution of the N crenelations in series. Note that we incorporate the inhomogeneous doping of the corrugation induced by its topography. Also, we add the diffusive

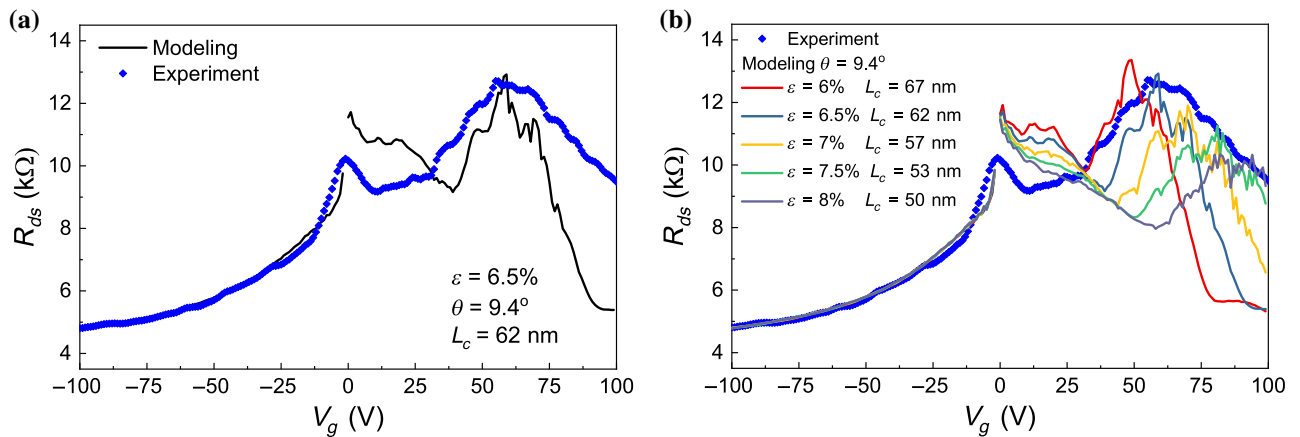


FIG. 4. A comparison between experiment and theory. (a) A comparison between the measured R_{ds} (blue symbols) at $T = 4.4$ K and $V_{ds} = 1$ mV and the calculated R_{ds} (black line) at $T = 0$ K at zero bias, as a function of V_g . Quantitative agreement is found for $\varepsilon = 6.5\%$, $L_{\text{strain}} = 62$ nm, the length of the barrier, and $\theta = 9.4^\circ$, the angle between the transport direction and the zigzag crystallographic direction of the graphene. (b) The measured R_{ds} (blue symbols) at $T = 4.4$ K and $V_{ds} = 1$ mV and the calculated R_{ds} (solid lines) at $T = 0$ K at zero bias, as a function of V_g for ε ranging from 6 to 8% and L_{strain} ranging from 50 to 67 nm.

contribution in unstrained-graphene regions, calculated from fits of the charge-neutrality point peak according to $R = R_c + L/(W|n|e\mu)$, where R_c is the contact resistance, n is the charge density of the graphene, and μ is the electron mobility over the entire structure, which includes the high-mobility regions on top of the crenulations and on suspended tensile graphene, as evidenced by the observation of Fabry-Perot oscillations in the R_{ds} - V_g characteristic and the low-mobility regions on the bottom of the crenulations (see Appendix C) [52].

In Fig. 4(a), we compare the measured resistance with the calculated resistance, taking ε , θ , and L_{barrier} (the length of the strain barriers) as adjustable parameters. From the position of the ancillary resistance peak, we deduce $\Delta V_{\text{strain}} = 163$ meV, corresponding to a longitudinal deformation $\varepsilon = 6\%$, consistent with geometrical considerations. From the magnitude of the ancillary peak, we extract $\theta = 9.4^\circ$ and $L_{\text{barrier}} = 62$ nm and $|A_\perp| = 126$ T\$\cdot\$nm, which is on the order of that produced by an external magnetic field $B \sim 2T$. The quantitative agreement between theory and experiment demonstrates a near-equal contribution of both the scalar and the pseudovector potentials, with $eV_F A_\perp = -126$ meV. We deduce at $E = \Delta V_{\text{strain}}$ authorized transmission angles of 57° for valley K and -57° for valley K' , which highlights a strong valley separation. It must be stressed that the experiments were performed at a temperature of 4.4 K and $eV_{ds} = 1$ meV, leading to $k_B T \sim 0.4$ meV $< eV_{ds} \ll \Delta V_{\text{strain}} \sim 163$ meV and $|eV_F A_\perp| \sim 126$ meV (estimated from our analysis). Based on these energy scales, we assume eV_{ds} and low temperature to have a minor impact on the calculated R_{ds} . However, we observe that the calculated ancillary resistance peak is narrower than that in the experimental data. We attribute this broadening to the strain heterogeneity

along a single barrier and the dispersion among the N crenulations in series, which are both incipient to our fabrication method. Nevertheless, the dispersion of strain remains modest, as a strain heterogeneity $\varepsilon = 6\text{--}9\%$ is sufficient to account for the broadening of the ancillary peak for $\theta = 9.4^\circ$, as observed in Fig. 4(b). The main objective of our analysis is to provide quantitative evidence for the balanced contribution of strain-induced scalar and pseudovector potentials on ballistic transport. On the other hand, considering that our theoretical description neglects some effects, such as the randomness of impurities, and that there are uncertainties on several factors, such as v_F , g_{strain} , and β , our estimates of θ and ε are approximate. This theoretical analysis provides a description of strain-barrier effects in the transmission of ballistic electrons and fully elucidates the origin of the ancillary resistance peak reported here.

We now discuss additional contributions to the observed phenomena. As we have already mentioned in Sec. I, strain in the present geometry can be described within a pseudovector potential. However, because of the uniaxial character of the strain field, which preserves the equivalence between the two triangular sublattices of graphene, there is no curl expected to arise that could give rise to Landau-level quantization. The latter has indeed been shown to be relevant in the case of a triangular strain field that breaks the sublattice symmetry [12]. In the present device, similar localized strain fields could be present in the case of some localized disorder. However, unless this disorder breaks time-reversal symmetry, it is not expected to yield significant deviations of the electrons from their trajectories. Indeed, a possible deviation of the trajectory of an electron in a particular valley should be compensated by that of an electron in the other valley, as a consequence of

time-reversal symmetry. Heavy processing of the bottom *h*-BN could induce a spatial variation in doping but a second auxiliary peak located at 163 meV would correspond to an extremely high doping value of $1.9 \times 10^{12} \text{ cm}^{-2}$, which seems unrealistic for charged impurities in *h*-BN [53]. A similar approach has been used by Sheng-Chin Ho *et al.* [23] to artificially create corrugated bilayer graphene and their work shows the existence of structured deformation in bilayer graphene. Finally, strain effects in the low-energy band structure of graphene also change the magnitude and isotropy of the Fermi velocity and thus in the density of states. However, the anisotropic renormalization of the Fermi velocity due to strain remains a second-order effect, neglected in this work [44]. Lastly, the electrostatic barrier effect due to distinct capacitances between the graphene regions on the top and bottom of the crenelation, which is otherwise included in our model, is too weak (< 7%) to be responsible on its own for a ΔV_{strain} of 163 meV [54,55].

V. CONCLUSIONS

In conclusion, using transport measurements at low temperature and microscopic modeling, we have investigated the Klein-tunneling transport of ballistic electrons across a series of strain-induced barriers. We have shown the existence of a large and broad ancillary resistance peak at a positive energy that originates from nearly equivalent contributions of strain-induced scalar and pseudovector potentials in strained barriers. Our study also reveals the quantum interference of ballistic electrons between strained-graphene barriers. Our platform based on crenelated *h*-BN/graphene heterostructures hopefully paves the way toward the realization of graphene quantum strain devices. It comprises the realization of high on-off transistors driven by a simple gate voltage resulting from the quantum nature of the transport without the need of a band gap and the implementation of valleytronics (filters and polarizers) as electrons belonging to each valley in our strained device are collimated by strained barriers in different directions [56]. Moreover, in our *h*-BN/graphene crenelated heterostructure, the charge carriers undergo a submicron periodic angular motion, which should lead to the emission of electromagnetic radiation in the terahertz spectral range, hopefully paving the way toward the development of integrated synchrotron-like terahertz emitters based on 2D materials. For basic science, this platform gives opportunities to develop strain engineering in a wide variety of 2D materials and van der Waals heterostructures, such as in twisted-bilayer graphene or in transition-metal dichalcogenides [57], with the aim of manipulating their electronic and optical properties and exploring new physical phenomena.

Note added. We recently became aware of a work addressing similar strained-junction physics [58].

ACKNOWLEDGMENTS

We thank J. Tignon, J. Torres, F. Teppe, P. Legagneux, P. Seneor, B. Dlubak, and M. B. Martin for fruitful discussions. This project has received funding from the European Research Council (ERC) under the European Union Horizon 2020 research and innovation program (Grant Agreement No. 820133). This research is supported by a public grant overseen by the French National Research Agency (ANR) as STEM2D (Grant No. ANR-19-CE24-0015).

APPENDIX A: DEVICE FABRICATION

To fabricate the crenelated *h*-BN/graphene heterostructure, we transferred a 62-nm-thick exfoliated *h*-BN flake on a silicon substrate with 500 nm of oxide by using the polymer-based dry pick-up and transfer technique. We etched trenches in the *h*-BN flake of depth 35 nm by using electron-beam lithography and reactive ion etching. To remove residues of the PMMA resin on the crenelated *h*-BN, it was submitted to an O₂ plasma cleaner. We also used the polymer-based dry pick-up and transfer technique to assemble a thin *h*-BN flake (8 nm) and exfoliated graphene and to transfer them onto the patterned *h*-BN. Afterward, we contacted the crenelated graphene with one-dimensional “edge contacts” to design source and drain electrodes by using electron-beam lithography, reactive ion etching, and the deposition of Cr(5 nm)/Au(50 nm). To access the silicon that is used as a back gate, we patterned an electrical access through SiO₂ by using laser lithography, reactive ion etching, and the deposition of Cr(5 nm)/Au(180 nm). At the end, the crenelated graphene transistor was $L = 12 \mu\text{m}$ long and $W = 8 \mu\text{m}$ wide and consisted of ten crenelations of length $l = 1 \mu\text{m}$ (i.e., with a 1 μm periodicity) and of two unstrained-graphene regions of length 1 μm at the ends.

APPENDIX B: MEASUREMENTS

The AFM measurements were performed in air, using silicon cantilevers operated in tapping mode. The Raman-spectroscopy measurements were performed with a Renishaw inVia Raman microscope with a 100 \times objective lens and at an excitation wavelength of 532 nm. For transport measurements, the sample was cooled down in a variable-temperature (4–300 K) liquid ⁴He cryostat. An ac voltage of 1 mV amplitude at a frequency $f = 77 \text{ Hz}$ and a dc voltage V_{ds} were applied between the source and drain electrodes, whereas a dc voltage V_g was applied to the gate. The ac signal was measured with a lock-in amplifier.

APPENDIX C: DIFFUSIVE CONTRIBUTION MODELING

To model the diffusive contribution to the resistance of our device, we used a capacitance calculated with the

average distance to the gate, $C_{av} = 6.1 \times 10^{-9}$ F cm $^{-2}$. The charge-carrier density n is then given by $|n| = \sqrt{(C(V_g - V_0)/e)^2 + n_0^2}$, where V_0 is a shift of the charge-neutrality point due to intrinsic doping of the sample, n_0 is a residual charge-carrier density, and C is the gate capacitance. The diffusive contribution in unstrained-graphene regions was calculated from fits of the charge-neutrality point peak according to $R = R_c + L/(W|n|e\mu)$, where R_c is the contact resistance, μ is the electron mobility over the entire structure, including unstrained areas—in which the mobility is assumed to be high, as evidenced by the observation of Fabry-Perot oscillations in the R_{ds} - V_g characteristics—and strained barriers, and n is the charge density of the graphene. We found $R_{\text{contact}} = 4288$ Ω and $n_0 = 4.5 \times 10^{11}$ cm $^{-2}$, which is the order of magnitude expected for such graphene flakes. The overall electronic mobility is 3604 cm $^{-2}$ V $^{-1}$ s $^{-1}$ if we consider the total length of the device (i.e., 12 μm). It should be pointed out that in addition to the presumed high-mobility unconstrained regions, the electron-mobility value includes ten strained barriers of similar length that strongly disrupt carrier transport.

-
- [1] D. Zhai and N. Sandler, Electron dynamics in strained graphene, *Mod. Phys. Lett. B* **33**, 1930001 (2019).
 - [2] C. Si, Z. Sun, and F. Liu, Strain engineering of graphene: A review, *Nanoscale* **8**, 3207 (2016).
 - [3] A. L. Kitt, V. M. Pereira, A. K. Swan, and B. B. Goldberg, Lattice-corrected strain-induced vector potentials in graphene, *Phys. Rev. B* **85**, 115432 (2012).
 - [4] A. McRae, G. Wei, and A. Champagne, Graphene quantum strain transistors, *Phys. Rev. Appl.* **11**, 054019 (2019).
 - [5] A. R. Botello-Méndez, J. C. Obeso-Jureidini, and G. G. Naumis, Toward an accurate tight-binding model of graphene's electronic properties under strain, *J. Phys. Chem. C* **122**, 15753 (2018).
 - [6] G. Montambaux, F. Piéchon, J.-N. Fuchs, and M. O. Goerbig, Merging of Dirac points in a two-dimensional crystal, *Phys. Rev. B* **80**, 153412 (2009).
 - [7] G. Montambaux, F. Piéchon, J.-N. Fuchs, and M. O. Goerbig, A universal Hamiltonian for motion and merging of Dirac points in a two-dimensional crystal, *Europhys. J. B* **72**, 509 (2009).
 - [8] V. M. Pereira, A. C. Neto, and N. Peres, Tight-binding approach to uniaxial strain in graphene, *Phys. Rev. B* **80**, 045401 (2009).
 - [9] V. M. Pereira and A. C. Neto, Strain engineering of graphene's electronic structure, *Phys. Rev. Lett.* **103**, 046801 (2009).
 - [10] F. Guinea, M. I. Katsnelson, and M. A. H. Vozmediano, Midgap states and charge inhomogeneities in corrugated graphene, *Phys. Rev. B* **77**, 075422 (2008).
 - [11] M. A. Vozmediano, M. Katsnelson, and F. Guinea, Gauge fields in graphene, *Phys. Rep.* **496**, 109 (2010).
 - [12] N. Levy, S. Burke, K. Meaker, M. Panlasigui, A. Zettl, F. Guinea, A. C. Neto, and M. F. Crommie, Strain-induced

pseudo-magnetic fields greater than 300 tesla in graphene nanobubbles, *Science* **329**, 544 (2010).

- [13] Y. Liu, J. N. B. Rodrigues, Y. Z. Luo, L. Li, A. Carvalho, M. Yang, E. Laksono, J. Lu, Y. Bao, H. Xu, S. J. R. Tan, Z. Qiu, C. H. Sow, Y. P. Feng, A. H. C. Neto, S. Adam, J. Lu, and K. P. Loh, Tailoring sample-wide pseudo-magnetic fields on a graphene–black phosphorus heterostructure, *Nat. Nanotechnol.* **13**, 828 (2018).
- [14] C.-C. Hsu, M. L. Teague, J.-Q. Wang, and N.-C. Yeh, Nanoscale strain engineering of giant pseudo-magnetic fields, valley polarization, and topological channels in graphene, *Sci. Adv.* **6**, eaat9488 (2020).
- [15] B. Uchoa and Y. Barlas, Superconducting states in pseudo-Landau-levels of strained graphene, *Phys. Rev. Lett.* **111**, 046604 (2013).
- [16] F. Xu, P.-H. Chou, C.-H. Chung, T.-K. Lee, and C.-Y. Mou, Strain-induced superconducting pair density wave states in graphene, *Phys. Rev. B* **98**, 205103 (2018).
- [17] A. Reserbat-Plantey, D. Kalita, Z. Han, L. Ferlazzo, S. Autier-Laurent, K. Komatsu, C. Li, R. Weil, A. Ralko, L. Marty, S. Guérion, N. Bendjab, H. Bouchiat, and V. Bouchiat, Strain superlattices and macroscale suspension of graphene induced by corrugated substrates, *Nano Lett.* **14**, 5044 (2014).
- [18] M. Goldsche, J. Sonntag, T. Khodkov, G. J. Verbiest, S. Reichardt, C. Neumann, T. Ouaj, N. von den Driesch, D. Buca, and C. Stampfer, Tailoring mechanically tunable strain fields in graphene, *Nano Lett.* **18**, 1707 (2018).
- [19] F. Anwar, C. Carlos, V. Saraswat, V. Mangu, M. Arnold, and F. Cavallo, Nanoscale graphene/Ge wigglers as building blocks for THz sources, *AIP Adv.* **7**, 115015 (2017).
- [20] Y. Jiang, J. Mao, J. Duan, X. Lai, K. Watanabe, T. Taniguchi, and E. Y. Andrei, Visualizing strain-induced pseudomagnetic fields in graphene through an hBN magnifying glass, *Nano Lett.* **17**, 2839 (2017).
- [21] H. Tomori, A. Kanda, H. Goto, Y. Ootuka, K. Tsukagoshi, S. Moriyama, E. Watanabe, and D. Tsuya, Introducing nonuniform strain to graphene using dielectric nanopillars, *Appl. Phys. Express* **4**, 075102 (2011).
- [22] A. Reserbat-Plantey, D. Kalita, Z. Han, L. Ferlazzo, S. Autier-Laurent, K. Komatsu, C. Li, R. Weil, A. Ralko, L. Marty, et al., Strain superlattices and macroscale suspension of graphene induced by corrugated substrates, *Nano Lett.* **14**, 5044 (2014).
- [23] S.-C. Ho, C.-H. Chang, Y.-C. Hsieh, S.-T. Lo, B. Huang, T.-H.-Y. Vu, C. Ortix, and T.-M. Chen, Hall effects in artificially corrugated bilayer graphene without breaking time-reversal symmetry, *Nat. Electron.* **4**, 116 (2021).
- [24] X. He, N. Tang, X. Sun, L. Gan, F. Ke, T. Wang, F. Xu, X. Wang, X. Yang, W. Ge, et al., Tuning the graphene work function by uniaxial strain, *Appl. Phys. Lett.* **106**, 043106 (2015).
- [25] L. Wang, A. Baumgartner, P. Makk, S. Zihlmann, B. S. Varghese, D. I. Indolese, K. Watanabe, T. Taniguchi, and C. Schönenberger, Global strain-induced scalar potential in graphene devices, *Commun. Phys.* **4**, 147 (2021).
- [26] H. Shioya, S. Russo, M. Yamamoto, M. F. Craciun, and S. Tarucha, Electron states of uniaxially strained graphene, *Nano Lett.* **15**, 7943 (2015).
- [27] S. Morikawa, Q. Wilmarth, S. Masubuchi, K. Watanabe, T. Taniguchi, B. Plaçais, and T. Machida, Dirac fermion

- reflector by ballistic graphene sawtooth-shaped npn junctions, *Semicond. Sci. Technol.* **32**, 045010 (2017).
- [28] C. R. Dean, A. F. Young, I. Meric, C. Lee, L. Wang, S. Sorgenfrei, K. Watanabe, T. Taniguchi, P. Kim, K. L. Shepard, *et al.*, Boron nitride substrates for high-quality graphene electronics, *Nat. Nanotechnol.* **5**, 722 (2010).
- [29] K. I. Bolotin, K. J. Sikes, J. Hone, H. L. Stormer, and P. Kim, Temperature-dependent transport in suspended graphene, *Phys. Rev. Lett.* **101**, 096802 (2008).
- [30] A. C. Ferrari and D. M. Basko, Raman spectroscopy as a versatile tool for studying the properties of graphene, *Nat. Nanotechnol.* **8**, 235 (2013).
- [31] J. E. Lee, G. Ahn, J. Shim, Y. S. Lee, and S. Ryu, Optical separation of mechanical strain from charge doping in graphene, *Nat. Commun.* **3**, 1 (2012).
- [32] X. Wang, K. Tantiwanichapan, J. W. Christopher, R. Paiella, and A. K. Swan, Uniaxial strain redistribution in corrugated graphene: Clamping, sliding, friction, and 2D band splitting, *Nano Lett.* **15**, 5969 (2015).
- [33] See the Supplemental Material at <http://link.aps.org-supplemental/10.1103/PhysRevApplied.22.024076> for additional information on the deconvoluted Raman spectra, the tight-binding calculation, and transport across a barrier of strained graphene.
- [34] L. Wang, I. Meric, P. Huang, Q. Gao, Y. Gao, H. Tran, T. Taniguchi, K. Watanabe, L. Campos, D. Muller, *et al.*, One-dimensional electrical contact to a two-dimensional material, *Science* **342**, 614 (2013).
- [35] A. Pierret, D. Mele, H. Graef, J. Palomo, T. Taniguchi, K. Watanabe, Y. Li, B. Toury, C. Journet, P. Steyer, V. Garnier, A. Loiseau, J.-M. Berroir, E. Bocquillon, G. Fèvre, C. Voisin, E. Baudin, M. Rosticher, and B. Plaçais, Dielectric permittivity, conductivity and breakdown field of hexagonal boron nitride, *Mater. Res. Express* **9**, 065901 (2022).
- [36] P. Huang, E. Riccardi, S. Messelot, H. Graef, F. Valmorra, J. Tignon, T. Taniguchi, K. Watanabe, S. Dhillon, B. Plaçais, *et al.*, Ultra-long carrier lifetime in neutral graphene-hBN van der Waals heterostructures under mid-infrared illumination, *Nat. Commun.* **11**, 1 (2020).
- [37] Q. Wilmart, S. Berrada, D. Torrin, V. H. Nguyen, G. Fèvre, J.-M. Berroir, P. Dollfus, and B. Plaçais, A Klein-tunneling transistor with ballistic graphene, *2D Mater.* **1**, 011006 (2014).
- [38] H. Graef, Q. Wilmart, M. Rosticher, D. Mele, L. Banszerus, C. Stampfer, T. Taniguchi, K. Watanabe, J. M. Berroir, E. Bocquillon, G. Fèvre, E. H. T. Teo, and B. Plaçais, A corner reflector of graphene Dirac fermions as a phonon-scattering sensor, *Nat. Commun.* **10**, 2428 (2019).
- [39] A. F. Young and P. Kim, Quantum interference and Klein tunnelling in graphene heterojunctions, *Nat. Phys.* **5**, 222 (2009).
- [40] P. Rickhaus, R. Maurand, M.-H. Liu, M. Weiss, K. Richter, and C. Schönenberger, Ballistic interferences in suspended graphene, *Nat. Commun.* **4**, 2342 (2013).
- [41] C. Déprez, L. Veyrat, H. Vignaud, G. Nayak, K. Watanabe, T. Taniguchi, F. Gay, H. Sellier, and B. Sacépé, A tunable Fabry-Pérot quantum Hall interferometer in graphene, *Nat. Nanotechnol.* **16**, 555 (2021).
- [42] J. L. Manes, Symmetry-based approach to electron-phonon interactions in graphene, *Phys. Rev. B* **76**, 045430 (2007).
- [43] H. Suzuura and T. Ando, Phonons and electron-phonon scattering in carbon nanotubes, *Phys. Rev. B* **65**, 235412 (2002).
- [44] S.-M. Choi, S.-H. Jhi, and Y.-W. Son, Effects of strain on electronic properties of graphene, *Phys. Rev. B* **81**, 081407 (2010).
- [45] F. Guinea, A. Geim, M. Katsnelson, and K. Novoselov, Generating quantizing pseudomagnetic fields by bending graphene ribbons, *Phys. Rev. B* **81**, 035408 (2010).
- [46] J. V. Sloan, A. A. P. Sanjuan, Z. Wang, C. Horvath, and S. Barraza-Lopez, Strain gauge fields for rippled graphene membranes under central mechanical load: An approach beyond first-order continuum elasticity, *Phys. Rev. B* **87**, 155436 (2013).
- [47] M. Schneider, D. Faria, S. V. Kusminskiy, and N. Sandler, Local sublattice symmetry breaking for graphene with a centrosymmetric deformation, *Phys. Rev. B* **91**, 161407 (2015).
- [48] O. Blakslee, D. Proctor, E. Seldin, G. Spence, and T. Weng, Elastic constants of compression-annealed pyrolytic graphite, *J. Appl. Phys.* **41**, 3373 (1970).
- [49] M. Fogler, F. Guinea, and M. Katsnelson, Pseudomagnetic fields and ballistic transport in a suspended graphene sheet, *Phys. Rev. Lett.* **101**, 226804 (2008).
- [50] Z.-Z. Cao, Y.-F. Cheng, and G.-Q. Li, Strain-controlled electron switch in graphene, *Appl. Phys. Lett.* **101**, 253507 (2012).
- [51] F. Wan, X. R. Wang, L. H. Liao, J. Y. Zhang, M. N. Chen, G. H. Zhou, Z. B. Siu, M. B. A. Jalil, and Y. Li, Valley-dependent transport in strain engineering graphene heterojunctions, *Chin. Phys. B* **31**, 077302 (2022).
- [52] N. W. Ashcroft and N. D. Mermin, *Solid State Physics* (Saunders College, Philadelphia, Pennsylvania, 1976).
- [53] A. C. Betz, S. H. Jhang, E. Paluszak, R. Ferreira, G. Fèvre, J.-M. Berroir, and B. Plaçais, Supercollision cooling in undoped graphene, *Nat. Phys.* **9**, 109 (2013).
- [54] M. Drienovsky, J. Joachimsmeyer, A. Sandner, M.-H. Liu, T. Taniguchi, K. Watanabe, K. Richter, D. Weiss, and J. Eroms, Commensurability oscillations in one-dimensional graphene superlattices, *Phys. Rev. Lett.* **121**, 026806 (2018).
- [55] P. Solís-Fernández, S. Okada, T. Sato, M. Tsuji, and H. Ago, Gate-tunable Dirac point of molecular doped graphene, *ACS Nano* **10**, 2930 (2016).
- [56] H. Yu, A. Kutana, and B. I. Yakobson, Electron optics and valley Hall effect of undulated graphene, *Nano Lett.* **22**, 2934 (2022).
- [57] Z. Peng, X. Chen, Y. Fan, D. J. Srolovitz, and D. Lei, Strain engineering of 2D semiconductors and graphene: From strain fields to band-structure tuning and photonic applications, *Light Sci. Appl.* **9**, 190 (2020).
- [58] A. C. McRae, G. Wei, L. Huang, S. Yigen, V. Tayari, and A. R. Champagne, Mechanical control of quantum transport in graphene, *Adv. Mater.* **36**, 2313629 (2024).
- [59] M. O.-L. Xerardo G Naumis, Salvador Barraza-Lopez, and H. Terrones, Electronic and optical properties of strained graphene and other strained 2D materials: A review, *Rep. Prog. Phys.* **80**, 096501 (2017).